Chemical Engineering Science 218 (2020) 115577

Contents lists available at ScienceDirect

Chemical Engineering Science

journal homepage: www.elsevier.com/locate/ces

An LBM-PNM framework for immiscible flow: With applications to droplet spreading on porous surfaces

Si Suo [a], Mingchao Liu [b,c], Yixiang Gan [a,*]

[a] School of Civil Engineering, The University of Sydney, NSW 2006, Australia
[b] Mathematical Institute, University of Oxford, Oxford OX2 6GG, United Kingdom
[c] Department of Engineering Mechanics, CNMM & AML, Tsinghua University, Beijing 100084, China

HIGHLIGHTS

- A robust algorithm coupling LBM and PNM was developed for modelling two-phase flow.
- The proposed algorithm has been validated against the experimental observation.
- The competition between droplet spreading and matrix imbibition was further studied.

GRAPHICAL ABSTRACT

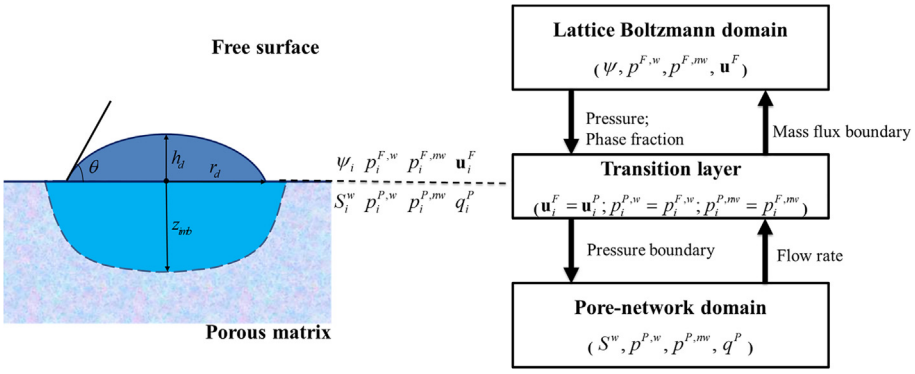

ARTICLE INFO

Article history:
Received 11 October 2019
Received in revised form 10 February 2020
Accepted 14 February 2020
Available online 14 February 2020

Keywords:
Multiphase flow
Multiscale modelling
Lattice Boltzmann method
Pore-network method
Droplet behaviour

ABSTRACT

The behaviour of droplets on porous media, combining the spreading above and imbibition into the medium, is of foundational interests for a series of applications. In this work, we combine the lattice Boltzmann method (LBM) and pore-network method (PNM) to develop an efficient and robust numerical framework in which the coarse-scale multiphase transport in porous media are modelled by the PNM while the fluid dynamics containing multiple components are resolved by the LBM. An effective transport mechanism has been implemented to ensure mass conservation and pressure continuity across the interface. This method is ideally adapted to flow domains, with two distinguishable characteristic length-scales. The numerical framework is validated by comparison with experimental observations of droplets on flat porous surfaces. Moreover, the behaviour of droplets on non-flat porous surfaces has been also investigated, demonstrating the influence of surface curvature on the competing mechanisms of droplet spreading and imbibition.

1. Introduction

The spreading and imbibition of droplets on porous media are commonly observed (Denesuk et al., 1994; Neogi and Miller, 1983), and encountered in various industrial situations, such as enhanced oil recovery (Perazzo et al., 2018), inkjet printing (Daniel and Berg, 2006; Wijshoff, 2018; Zhou et al., 2017), film coating (Christodoulou et al., 2018), and cultural heritage conservation (Bakhta et al., 2019; Camuffo, 2013). A clear understanding of the interaction between droplets and porous substrates is essential for the industrial application, and, as such, a series of

* Corresponding author.
E-mail address: yixiang.gan@sydney.edu.au (Y. Gan).

https://doi.org/10.1016/j.ces.2020.115577
0009-2509/

Nomenclature list

A_L	Cross-section area
Bo	Bond number
$\boldsymbol{B_{drag}}$	Drag force
$\boldsymbol{c}$	Particle velocity vector
C	Interface property parameter
$\boldsymbol{d}$	Unit directional vector of throat
$\boldsymbol{e}$	Discrete particle velocity
f	Density distribution function
$\boldsymbol{F_{ext}}$	External body force
G	Vertical body force
h_d	Droplet height
$\boldsymbol{I}$	Unit tensor
k	Pore throat conductivity
L	Length scale
l_L	Lattice space
m	Mass
$\boldsymbol{n}$	Normal vector
p	Fluid pressure
q	Flow rate
r_d	Droplet radius
S	Pore saturation
t	Time
$\boldsymbol{u}$	Velocity vector
V	Volume of pore body
V_{imb}	Infiltration volume
w	Weighting factor
z_{imb}	Vertical imbibition depth

Greek symbols

α	Tip angle
β	Interface thickness adjusting parameter
φ	Color flux angle
θ	Contact angle
ϕ	Porosity
ν	Fluid viscosity
ω	Relaxation rate
$\boldsymbol{\varepsilon}$	Rate of shear strain tensor
ρ	Fluid density
ψ	Phase fraction
σ	Surface tension
η	Dynamic viscosity
Π	Collision operator
τ	Tangential vector
$\boldsymbol{\Omega}$	Flow domain
$\boldsymbol{\Gamma}$	Interface boundary

Subscripts and superscripts

c	Capillary
eq	Equilibrium
nw	Non-wetting fluid component
w	Wetting fluid component
int	Interface
$wall$	Solid wall
$\boldsymbol{P}$	Porous matrix
$\boldsymbol{F}$	Free surface
L	LBM
$*$	Post-collision
$**$	Post-recolouring
$+$	Symmetry part
$-$	Anti-symmetry

investigations have been conducted experimentally and numerically on the mechanism of droplet spreading and imbibition on flat porous surfaces. The pioneering work (Denesuk et al., 1994) focused on solving a mathematical model of the problem and suggests that the behaviour of droplet on porous substrate is influenced by both viscous spreading and capillary infiltration. This suggestion has been verified by several experimental works (Clarke et al., 2002; Oko et al., 2014; Starov et al., 2003). Recently, Léang et al. (2019) have presented direct visualisations of not only the droplets outside the porous matrix but also of the wet zone inside during the imbibition process. Furthermore, these experimental results highlight a universal law for the interplay between different porous layers and droplets.

In the meantime, in order to further understand the mechanism of the interaction between liquids and porous media, various numerical approaches have been developed. Generally, simulations of this problem can be classified into two categories: continuum scale and pore scale. For continuum-scale modelling, fluid flow (outside a porous medium) is generally governed by the incompressible Navier-Stokes (NS) equations, i.e.,

$$\nabla \cdot \boldsymbol{u} = 0, \tag{1}$$

$$\rho\left[\frac{\partial \boldsymbol{u}}{\partial t} + \boldsymbol{u}\cdot\nabla\boldsymbol{u}\right] = \nabla\cdot[-p\boldsymbol{I} + 2\mu\boldsymbol{\varepsilon}] + \boldsymbol{F_{ext}}, \tag{2}$$

where ρ and μ are the fluid density and dynamic viscosity, respectively, $\boldsymbol{u}$ the velocity vector, $\boldsymbol{I}$ the unit tensor, $\boldsymbol{\varepsilon}$ the rate of shear strain tensor, p the fluid pressure, and $\boldsymbol{F_{ext}}$ the external volume force. Simultaneously, the Brinkman/Darcy-modified scheme is adopted for flows inside porous media, i.e. (Hsu and Cheng, 1990),

$$\nabla \cdot \boldsymbol{u} = 0, \tag{3}$$

$$\rho\left[\frac{\partial \boldsymbol{u}}{\partial t} + \boldsymbol{u}\cdot\nabla\frac{\boldsymbol{u}}{\phi}\right] = \nabla\cdot[-\phi p\boldsymbol{I} + 2\mu\boldsymbol{\varepsilon}] + \boldsymbol{B_{drag}} + \boldsymbol{F_{ext}}, \tag{4}$$

where ϕ is the porosity, and $\boldsymbol{B_{drag}}$ is the drag force per unit volume. These two flow domains are linked by continuity conditions at the interface (Fu et al., 2019; Tan, 2017). Nevertheless, although the porosity and drag effect are considered in the Brinkman/Darcy-modified scheme, the pore-scale details of porous matrix are ignored. In particular, this framework cannot describe the capillary effect exactly, especially for extremely slow capillary flow in complex porous geometry (Qin et al., 2019), where surface tension leads to a capillary pressure depending on the pore-scale meniscus curvature. Another limitation of this numerical framework is that only the porous surface wettability can be considered while the wettability of the internal porous material cannot. Therefore, when the wettability of the inner porous material and of the porous surface are in contrast, e.g., water droplets on hydrophilic fibre mats with a surface contact angle of more than 120° due to the surface roughness (Wang et al., 2016b), this theoretical framework is not capable of properly describing the flow.

Compared with the continuum-scale modelling, pore-level simulations have been expected for detailed insights of droplet imbibition inside the porous matrix, and based on the NS equations and interface-tracking techniques, pore-scale modelling releases the limitation of assumptions used in Eq. (4). Among various numerical methods, such as molecular dynamics (MD) (Pham et al., 2018), smoothed particle hydrodynamics (SPH) (Meng et al., 2014) and volume of fluid method (VOF) (Das et al., 2018), the lattice Boltzmann method (LBM) has been growing as a mature tool to simulate multi-phase/component flows over past decades. Contrary to the traditional interface-tracking techniques including the level-set method and the phase-field method, LB models can naturally

describe the interface evolution since they are based on the Boltzmann's kinetic theory and the fundamental Boltzmann equations originate from molecular kinetics which effectively characterize the moving interfaces among phases. Recently, LBM-based simulation works about droplet behaviours on various porous media, e.g., random fibrous composites (Bakhta et al., 2019) and capillary tube arrays (Frank and Perre, 2012), has been reported. However, like other pore-scale numerical frameworks, LBM also suffers from the high consumption of computing resources and thus it is only suitable for the case with similar size of pore size and droplet size.

Noteworthily, as a representative pore-scale method, the pore-network method (PNM), distinguished by its high computational efficiency, has been successfully employed in multiphase flow systems (Blunt, 2001), though simplified pore structures and flow mechanisms are usually assumed. At present, the PNM alone can be used to simulate the behaviour of droplets on porous media only under the assumption that the base radius of a droplet keeps constant during the imbibition process, and thus fluid flow outside the porous matrix should be neglected (Markicevic et al., 2009; Markicevic and Navaz, 2010; Yin et al., 2018).

In the past decades, various numerical methods have been developed and adopted for simulating multi-phase/component flows. However, the applications of current numerical frameworks as summarized above in multiscale flow problems are still limited by low numerical efficiency or accuracy. As a typical multiscale problem, the simulation of droplet spreading on porous media requires to treat flow domains with two distinguishable characteristic length-scales, i.e., outside and inside porous media. To meet such requirement, coupling LBM and PNM can be a potential solution, where fluid transport in porous media is modelled by the PNM while the outside multicomponent flow is resolved by the LBM. This solution firstly provides a complementary function in areas where continuum- or pore-scale modelling is lacking because both LBM and PNM are pore-scale modelling methods with good numerical accuracy and the porous zone is represented by pore-throat network guaranteeing the numerical efficiency. Above all, it is compatible to synergize these two methods. Specifically, on time evolution, both methods adopt the explicit scheme; on space discretization, PNM can be straightforwardly adapted to the stair-wise boundary of LBM due to the simple pore-throat topology of PNM. However, despite the clear potential and applications discussed above, such coupling between LBM and PNM for multiphase flow problems has not been done before, which motivates the development here in this paper with applications towards studying the droplet dynamics on porous surfaces, including the concurrent spreading and imbibition processes.

In this work, we use an LBM-PNM coupling technique to develop a robust numerical framework suitable to describe the two-phase flow in the domain with two highly contrasting length scales. We validate our method by comparison with available experimental results of droplet interacting with a flat porous surface from literature. Beyond validation, we extend our method to more general situations by considering a droplet on a non-flat porous surface.

2. Numerical framework

In this section, we first introduce the multi-component LBM and PNM adopted in this study, separately; then the coupling technique between the pure fluid flow and the flow in porous media is elaborated.

2.1. Multi-component lattice Boltzmann method

There have been many multi-component schemes based on the LBM, including the Shan-Chen model (Shan and Chen, 1993), free-energy model (Swift et al., 1996), and Rothman-Keller model (R-K model) (Rothman and Keller, 1988). Although the Shan-Chen model is the simplest one, it always suffers from stability issues (Huang et al., 2011). Proposed by Rothman and Keller (Rothman and Keller, 1988) and further improved by Gunstensen et al (Gunstensen et al., 1991) who introduced the perturbation operator into the original LBM loop, the R-K model is able to handle various two-phase flows (Ba et al., 2016; Huang et al., 2014; Leclaire et al., 2013) and hence adopted in this study. Specifically, for two-phase flows, there are two particle distribution functions $f_i^w(\boldsymbol{x},t)$ and $f_i^{nw}(\boldsymbol{x},t)$ defined in the R-K model, where the superscript w and nw represent so-called wetting or non-wetting fluid components, respectively (Rothman and Keller, 1988).

Besides streaming and collision steps in the standard lattice Boltzmann method, a recolouring step is required for each component in the R-K model to ensure lattice can move between different components. Here, we simply illustrate how these three steps construct a loop and give certain details pertaining to each step. Assume the loop begins with streaming step,

$$f_i^k(\boldsymbol{x}+\boldsymbol{e}_i\delta t, t+\delta t) = f_i^{k**}(\boldsymbol{x},t), \tag{5}$$

where f_i^{k**} is post-recolouring particle distribution function for the k component, $\boldsymbol{e}_i$ is the discrete velocity set. For the lattice model, D2Q9, adopted in this study,

$$\boldsymbol{e}_i = c\begin{bmatrix} 0 & 1 & 0 & -1 & 0 & 1 & -1 & -1 & 1 \\ 0 & 0 & 1 & 0 & -1 & 1 & 1 & -1 & -1 \end{bmatrix}, \tag{6}$$

where $c=\delta x/\delta t$ is the lattice speed, and δx and δt are fixed as unity. Additionally, the lattice units including length l_L, time t_L, and mass m_L are adopted for convenience. Next, the collision step in R-K model (Latva-Kokko and Rothman, 2005) can be expressed as

$$f_i^{k*}(\boldsymbol{x},t) = f_i^k(\boldsymbol{x},t) + \Pi_{1i}^k + \Pi_{2i}^k, \tag{7}$$

where f_i^{k*} is post-collision particle distribution function for the k component. For the sake of numerical stability and efficiency, two-relaxation-time (TRT) scheme (Ginzburg et al., 2008a,b) is used as Π_{1i}^k,

$$\begin{aligned}\Pi_{1i}^k = &-\frac{\omega^{k+}}{2}\left(f_i^k - f_i^{k,eq} + f_{\bar{\imath}}^k - f_{\bar{\imath}}^{k,eq}\right) \\ &-\frac{\omega^{k-}}{2}\left(f_i^k - f_i^{k,eq} - f_{\bar{\imath}}^k + f_{\bar{\imath}}^{k,eq}\right),\end{aligned} \tag{8}$$

where ω^{k+} is the relaxation rate related to fluid viscosity $v^k = \left(\frac{1}{\omega^{k+}} - 0.5\right)/3$ and ω^{k-} is related to the numerical stability; $\bar{\imath}$ represents the opposite direction of i. The equilibrium distribution function $f_i^{k,eq}$ is calculated as

$$f_i^{k,eq} = \rho^k w_i\left[1 + \frac{\boldsymbol{e}_i\cdot\boldsymbol{u}}{c_s^2} + \frac{(\boldsymbol{e}_i\cdot\boldsymbol{u})^2}{2c_s^4} - \frac{|\boldsymbol{u}|^2}{2c_s^2}\right], \tag{9}$$

where ρ^k and $\boldsymbol{u}$ can be obtained by zero and first-order momentum of f_i^k,

$$\rho^k = \sum\nolimits_i f_i^k, \tag{10}$$

$$\rho = \sum\nolimits_k \rho^k, \text{ and} \tag{11}$$

$$\rho\boldsymbol{u} = \sum\nolimits_k\sum\nolimits_i\left(f_i^k\boldsymbol{e}_i\right). \tag{12}$$

Then, phase fraction ψ is defined as

$$\psi = \frac{\rho^w - \rho^{nw}}{\rho^w + \rho^{nw}} \in [-1,1]. \tag{13}$$

The perturbation operator, which contributes to the surface tension, Π_{2i}^{k}, as per the Reis and Phillips' scheme (Reis and Phillips, 2007),

$$\Pi_{2i}^{k}=\frac{C^{k}}{2}|\boldsymbol{q}_{c}|\left[w_{i}\frac{(\boldsymbol{e}_{i}\cdot\boldsymbol{q}_{c})^{2}}{|\boldsymbol{q}_{c}|^{2}}-B_{i}\right], \tag{14}$$

where $B_0=-4/27$, $B_{1\ 4}=-2/27$, and $B_{5\ 8}=-5/108$; $\boldsymbol{q}_{corlor}$ is the so-called colour flux and is calculated as

$$\boldsymbol{q}_{color}=\sum_{i}\boldsymbol{e}_{i}\left[f_{i}^{w}(x)-f_{i}^{nw}(x)\right]. \tag{15}$$

Finally, the recolouring step, which keeps two phases separated and immiscible, can be implemented as

$$f_{i}^{w**}=\frac{\rho^{w}}{\rho}\left(f_{i}^{w*}+f_{i}^{nw*}\right)+\beta\frac{\rho^{w}\rho^{nw}}{\rho^{2}}f_{i}^{eq}(\rho,0)cos(\varphi_{i}),\ \text{and} \tag{16}$$

$$f_{i}^{nw**}=\frac{\rho^{nw}}{\rho}\left(f_{i}^{w*}+f_{i}^{nw*}\right)+\beta\frac{\rho^{w}\rho^{nw}}{\rho^{2}}f_{i}^{eq}(\rho,0)cos(\varphi_{i}), \tag{17}$$

where φ_i is the angle between $\boldsymbol{q}_{color}$ and $\boldsymbol{e}_i$. The parameters C^k in Eq. (14) and β in Eqs. (16) and (17) determine the two-phase interfacial properties. Specifically, β, ranging from 0 to 1, is responsible for the interface thickness and set as 1 here; the surface tension σ is determined by C^k and ω^{k+}, and according to Ref. (Liu et al., 2012),

$$\sigma=\frac{4}{9}\frac{(C^{w}+C^{nw})}{(\omega^{w+}+\omega^{nw+})}. \tag{18}$$

2.2. Pore-network method

For two-phase flow, the porous media can be represented by a network composed of pore bodies and pore throats, both of which are filled with two types of fluids, i.e. the wetting or non-wetting phase. Each fluid component has its own pressure, i.e. p^w and p^{nw}, and these two pressures are connected by local capillary pressure-saturation relationship in pore bodies, i.e.,

$$p^{nw}=p^{w}+p^{c}(S^{w}), \tag{19}$$

where p^c is the pore capillary pressure depending on the saturation of the wetting phase S^w. According to the mass conservation law, the controlling equation of each pore are built as (Thompson, 2002),

$$\sum_{j}\left[\left(k_{ij}^{w}+k_{ij}^{nw}\right)\left(p_{i}^{w}-p_{j}^{w}\right)+k_{ij}^{nw}\left(p_{i}^{c}-p_{j}^{c}\right)\right]=0. \tag{20}$$

In Eq. (20), k_{ij}^{w} and k_{ij}^{nw} are the wetting and non-wetting phase conductivities of the throat connecting the pore i and the pore j. Then, the two-phase pressure field can be solved through a set of linear algebraic equations whose unknowns are wetting phase pressure p_i^w, as shown in Eq. (20). Finally, the state of each pore and throat is updated by

$$V_{i}\frac{\Delta S^{w}}{\Delta t}=\sum_{j}q_{ij}^{w}, \tag{21}$$

$$q_{ij}^{w}=k_{ij}^{w}\left(p_{j}^{w}-p_{i}^{w}\right) \tag{22}$$

where q_{ij} is the flow rate of throat j connected with pore i; V_i is the volume of pore body i.

The Eq. (20) is readily implemented as a numerical framework and it has been widely adopted in analysis of oil-water systems (Bauer et al., 2012; Blunt et al., 2013; Joekar-Niasar et al., 2013; Valvatne and Blunt, 2004). However, for some cases where the change of non-wetting phase pressure can be neglected, e.g., water-air imbibition, the above algorithm can be simplified (Yin et al., 2018). Assuming that the pressure of the non-wetting phase remains constant and uniform at each pore, for all of wetting-phase-saturated pores, the mass conservation equation can be expressed as

$$\sum_{j}k_{ij}^{w}\left(p_{i}^{w}-p_{j}^{w}\right)=0, \tag{23}$$

where the unknowns are the pressure of saturated pores while the pressure of unsaturated pores can be determined explicitly by Eq. (19) and thus act as known boundary values. Both local rules including the capillary pressure-saturation relationship for pore bodies, entry capillary pressure for pore throats, and snap-off rules, and the determination of pore throat conductivity are implemented as referred in the article of Joekar-Niasar et al. (2010).

2.3. LBM-PNM coupling technique

The porous medium with free surface is a typical heterogeneous system in which two flow fields with contrasting characteristic length scales, i.e., the porous matrix ($\boldsymbol{\Omega^P}$) and outside free surface ($\boldsymbol{\Omega^F}$) are connected. For pore-scale modelling, the connection between these two domains are naturally built up since a unified numerical method is used to solve two flow fields; whereas for continuum-scale modelling, a porous interface ($\boldsymbol{\Gamma}_{int}$) is generally introduced to deal with the continuity of mass flux and pressure across two domains, i.e., the relationship between velocities ($\boldsymbol{u}_{int}^{F}$ and $\boldsymbol{u}_{int}^{P}$) and pressures (p_{int}^{F} and p_{int}^{P}) at the interface, as shown in Fig. 1. The interface condition varies with flow situation and it is principally classified into two categories (Levy and Sanchez-Palencia, 1975): near parallel flow and near normal flow. For the case of near parallel flow, the interface condition is suggested as

$$\boldsymbol{u}_{int}^{F}=0; \tag{24}$$

$$p_{int}^{F}=p_{int}^{P}. \tag{25}$$

Eq. (24) originates from the continuity of mass flux by assuming the filtration velocity in porous media can be neglected, and thus the porous interface $\boldsymbol{\Gamma}_{int}$ can be treated as a no-slip boundary for $\boldsymbol{\Omega^F}$; then the pressure in $\boldsymbol{\Omega^F}$ is solved and transferred to $\boldsymbol{\Omega^P}$ as per the continuity of pressure i.e., Eq. (25) at the interface. For the case of near normal flow, the interface condition is suggested as

$$\boldsymbol{u}_{int}^{F}\cdot\boldsymbol{\tau}_{int}=0, \tag{26}$$

$$\boldsymbol{u}_{int}^{F}\cdot\boldsymbol{n}_{int}=\boldsymbol{u}_{int}^{P}\cdot\boldsymbol{n}_{int}, \tag{27}$$

$$p_{int}^{P}=Constant. \tag{28}$$

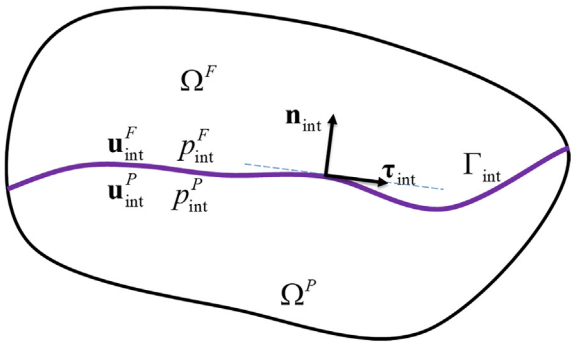

Fig. 1. Schematic of a typical two-domain system, containing the free surface domain ($\boldsymbol{\Omega^F}$) and the porous matrix ($\boldsymbol{\Omega^P}$) connected by porous interface ($\boldsymbol{\Gamma}_{int}$) with normal vector $\mathbf{n}_{int}$ and tangent vector τ_{int}.

By assigning the interface pressure of porous matrix a constant value, the flux $\boldsymbol{u}_{int}^{P}$ can be solved and transferred to pure fluid domain as per Eqs. (26) and (27), i.e., the mass conservation law. Therefore, the filtration velocity in porous matrix is of similar magnitude within pure fluid flow. However, the no-slip assumption, i.e., $\boldsymbol{u}_{int}^{F} \cdot \boldsymbol{\tau}_{int} = 0$, is adopted in the above two interface treatments, and such assumption is obviously inconsistent with the observation of droplet spreading behaviour on porous substrates since besides imbibition the contact line of droplet may be mobile along the porous surface, especially on a titled surface.

To simulate the dynamics of droplet on porous media precisely, the slip effect, i.e., the mobility of the contact line, on the surface should be considered whilst the mass conservation and pressure continuity should be guaranteed at the porous interface ($\boldsymbol{\Gamma}_i$). So, the generalised interface conditions adopted in this study can be expressed as

$$\boldsymbol{u}_{int}^{F} = \boldsymbol{u}_{int}^{P} \tag{29}$$

$$p_{int}^{P,w} = p_{int}^{F,w} \tag{30}$$

$$p_{int}^{P,nw} = p_{int}^{F,nw}, \tag{31}$$

where the superscripts w and nw represent wetting phase and non-wetting phase, respectively. For pure fluid domain ($\boldsymbol{\Omega}^{\boldsymbol{F}}$), the porous interface ($\boldsymbol{\Gamma}_{int}$) can be treated as a mass flux condition boundary, and the pressure field of $\boldsymbol{\Omega}^{\boldsymbol{F}}$ can be solved and transferred to porous matrix ($\boldsymbol{\Omega}^{\boldsymbol{P}}$) as per (30); then the mass flux at the interface $\boldsymbol{\Gamma}_{int}$ can be obtained and updated back to $\boldsymbol{\Omega}^{\boldsymbol{P}}$.

In the numerical implementation, as shown in Fig. 2(a), the free surface can be described through the LBM while the PNM being applied in porous matrix and a transition layer is set at the interface where lattices in LBM and pores in PNM share the same position. As for the topology, arbitrary connections between LBM and PNM domain, i.e., one lattice to none, one lattice to multiple pores, or multiple lattices to one pore, are allowed in this concurrent numerical framework, representing a variety of characteristic size contrast between the pure fluid flow field and the porous matrix. In another word, the proposed coupling technique can cover situations with $L^F/L^P \approx 1$, $L^F/L^P > 1$, and $L^F/L^P < 1$ with L^F and L^P being the representative physical lengths of pure fluid field and porous matrix, respectively. Whereas cases with $L^F/L^P << 1$ can be resolved with pure multi-component LBM (Bakhta et al., 2019; Frank and Perre, 2012). However, for cases with $L^F/L^P \approx 1$ or $L^F/L^P >> 1$, the current method can provide a unique and robust solution.

To numerically implement the coupling of LBM and PNM domains, Eq. (29) should be adapted as a discretised scheme. Specifically, the link between each component of flow velocity $\boldsymbol{u}_{int}^{F}$ and pore flow rate q_{int}^{P} can be established as,

$$\left(\boldsymbol{u}_{int}^{F} \cdot \boldsymbol{n}_{int}\right) \cdot \boldsymbol{n}_{int} \cdot A_L = \sum_j^{N_t} q_{ij}^{P} \cdot \left(\boldsymbol{d}_{ij} \cdot \boldsymbol{n}_{int}\right) \cdot \boldsymbol{n}_{int} \tag{32}$$

$$\left[\boldsymbol{u}_{int}^{F} - \left(\boldsymbol{u}_{int}^{F} \cdot \boldsymbol{n}_{int}\right) \cdot \boldsymbol{n}_{int}\right] \cdot A_L = \sum_j^{N_t} q_{ij}^{P} \cdot \left[\boldsymbol{d}_{ij} - \left(\boldsymbol{d}_{ij} \cdot \boldsymbol{n}_{int}\right) \cdot \boldsymbol{n}_{int}\right] \tag{33}$$

where N_t is the total number of the connected throats; $\boldsymbol{d}_{ij}$ is unit direction vector of throat ij, and A_L is the cross-section area between two lattices and equals l_L in 2D and l_L^2 in 3D. Eqs. (32) and (33) are in generalised form, i.e., suitable for both 2D and 3D situations, and specifically for 2D cases, only directions of normal $\boldsymbol{n}_{int}$ and tangent $\boldsymbol{\tau}_{int}$, as shown in Fig. 1, should be considered. Besides, the saturation of pores S_i^w and the phase fraction of lattices ψ_i, as defined in Eq. (13), on the transition layer should be linked as

$$S_i^w = \frac{(1+\psi_i)}{2} \tag{34}$$

In this numerical framework, wetting phenomena are simulated by setting fictitious wall densities ρ_{wall}^{w} and ρ_{wall}^{nw} on the transition layer, and the contact angle in the pure fluid region θ^F can be analytically determined (Huang et al., 2014) as

$$\cos\theta^F = \frac{\rho_{wall}^{w} - \rho_{wall}^{nw}}{\rho_{wall}^{w} + \rho_{wall}^{nw}} \in [-1, 1]. \tag{35}$$

For the porous matrix, the inside wettability can be measured by the determination of capillary pressure p^c in Eq. (19), and generally $p^c \propto \cos\theta^P$ (Joekar-Niasar et al., 2010), where θ^P is the contact angle in the porous matrix. From the above, our proposed coupling technique is featured by the convenience that the wetta-

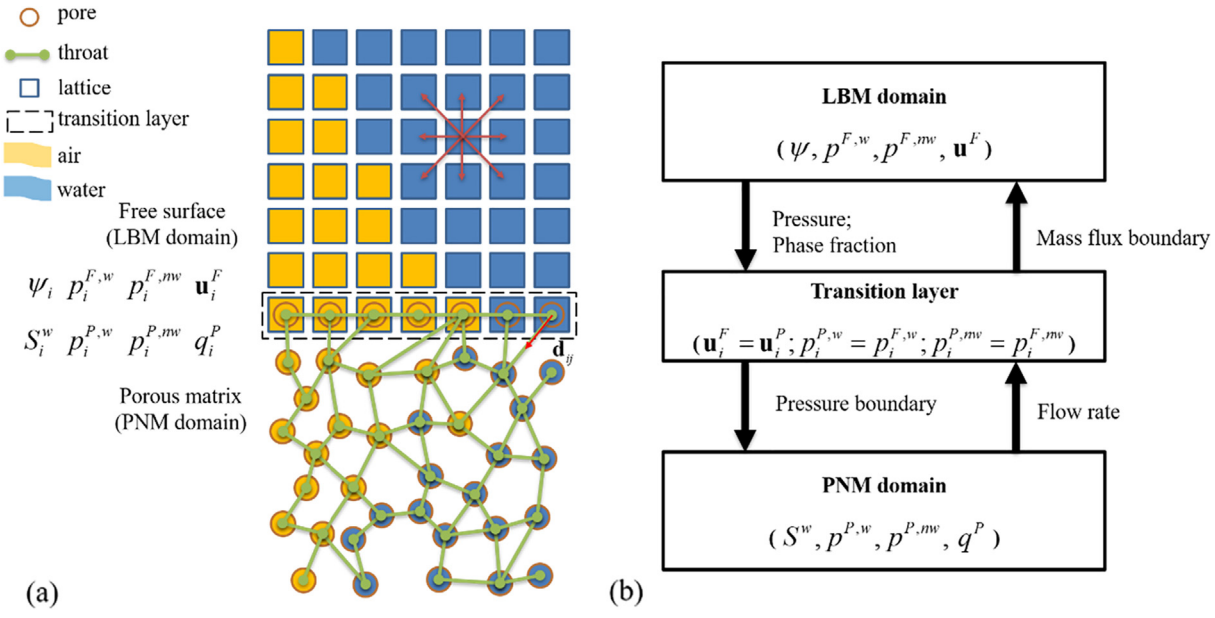

Fig. 2. (a) The schematic of the combination between LBM and PNM domains; (b) the flow chart of the interface treatment.

bility inside and outside porous region can be considered separately, and it is beyond the limitation of existed numerical framework that both θ^F and θ^P are required to be unified (Fu et al., 2019).

To concurrently couple these two methods, an important issue is time synchronisation since the proper time steps of LBM and PNM may be different. For LBM domain, the time step Δt_L is fixed as one; for PNM domain, the time step Δt_P varies with the fluid occupation state inside the pore. Specifically, every pore body possesses a local time step $\Delta t_{i,P}$ after which its saturation S^w would be 1 (imbibition path) or $S^w_{\min}$ (drainage path), and Δt_P is the minimum value of all local time steps. In this study, we take Δt_L as a reference time step and assume that the LBM domain remain unchanged during Δt_L. The actual time step $\bar{\Delta t}_P$ is determined as $\bar{\Delta t}_P = \min(\Delta t_P, \Delta t_L)$, suggesting that one main loop contains only one LBM loop but may contain more than one PNM loops. The specific algorithm can be referred to ***Appendix***.

It should be pointed out that for a sessile droplet, the current treatment is exact enough on mass conservation and pressure continuity as well as the shear stress effect in the free surface flow since the process is mostly controlled by capillary pressure and the outside flow is rather slow; however, for a dynamic droplet (with higher Ca number), e.g., droplet splashing on a porous surface, as one of our future topics, the shear stress would dominate the droplet behaviour due to the high velocity amplitude and an implicit loop of moment continuity for every time step may be needed to couple the domains. Special treatments should be taken in such dynamic conditions.

3. Validation and applications

In this section, we firstly validate the proposed numerical framework through modelling droplet spreading and imbibition on a flat porous surface and comparing against the available experimental observations. However, non-flat surfaces, e.g., rough surfaces, are more commonly encountered in nature. Besides the porosity and fluid properties, the surface topology should be another key factor of the droplet behaviour. Thus, after validation we generalise the simulations to focus more on the behaviour of a droplet on a non-flat porous surface to highlight the competition between the spreading and imbibition of the droplet.

3.1. Droplets on a porous substrate

The recent experimental work of Leang et al.'s work (Léang et al., 2019) provided a new imaging technique which simultaneously direct visualise droplet spreading and imbibition processes, enabling a clear possibility to validate our proposed LBM-PNM model in both free surface (resolved by LBM) and porous domains (by PNM) concurrently. The validations of each individual domain, against either theoretical or experimental approaches have been conducted in many previous studies (Clarke et al., 2002; Oko et al., 2014; Starov et al., 2003), thus were not included in our current manuscript. Here, using the proposed LBM-PNM framework, the imbibition process of water droplet on porous matrix is simulated within a 2D domain, shown in Fig. 3(a), where the upper part is the LBM part of 200×50 lattices with no-slip top wall and periodic left and right boundaries, while the rest is the PNM part of 200×100 pores with fixed pressure boundaries. The droplet within the LBM domain is initialised as the invading phase with contact angle $\theta_0 = 15^\circ$, droplet radius $r_{d0} = 22 l_L$, and droplet height $h_{d0} = 16 l_L$ located on the middle of the interface. Other flow conditions are listed as follows: relaxation rate $\omega_n = \omega_{nw} = 1$, surface tension $\sigma = 0.26 m_L \cdot t_L^{-2}$, external vertical body force $G = 5 \times 10^{-5} m_L \cdot t_L^{-2} \cdot l_L^{-2}$ (with the equivalent Bond number $Bo = 0.093$) acting as a downwards gravity term in the LBM domain. For the PNM domain, two kinds of pore-throat networks are homogeneously generated, i.e., the pores and throats have uniform properties with contrast permeability and porosity, (1) $k = 0.0079 l_L^2$, $\phi = 0.28$ and (2) $k = 0.016 l_L^2$, $\phi = 0.48$, corresponding to the characteristic features of the experimental cases named SM-30 and HS-40 in Ref (Léang et al., 2019), respectively, and these material parameters are listed in Table 1.

The evolutions of quantities including the vertical imbibition depth z_{imb}/h_{d0}, contact angle θ/θ_0, and dimensionless droplet radius $r_d/r_{d,\max}$ with time scaled by the Darcy's time, i.e., $t_{\text{Darcy}} = \eta \cdot h_{d0}^2 \cdot \phi/(k \cdot P_c)$, are presented in Fig. 3(b-d) and compared to the experimental data from Ref. (Léang et al., 2019). As shown in Fig. 3(b-d), most numerical results are in good agreement with the experimental results except the dimensionless apparent contact angle θ/θ_0, in particularly when $>30(t - t_0)/t_{\text{Darcy}}$. In experiments, the measurement of the contact angle can be easily affected by the exactness of contact line. However, a droplet tends to form a thin film after a certain time and the identification of contact line would be gradually ambiguous. Thus, there is obvious deviation for θ/θ_0 between the numerical results and experimental data. Overall, our results follow the universal behaviour demonstrated in Ref. (Léang et al., 2019). Furthermore, the proposed numerical framework can capture the intrinsic contact line dynamics of droplet on porous matrix.

3.2. Sessile droplets on porous tips

Having validated the proposed numerical framework, we extend the present work: besides flat porous surfaces, non-flat ones are more commonly encountered in nature, i.e., the rough surfaces (Keiser et al., 2019; Wang et al., 2016a). Sessile droplets on non-flat porous surfaces may introduce more complex interaction between spreading and imbibition processes. In this work, we only consider the situations that the size of droplet is comparable to the characteristic length of roughness, and the schematic of the simulation model is demonstrated in Fig. 4. To investigate the effect of curvature of the non-flat surface, including concave and convex cases, on the droplet behaviour, six geometries with different tip angle (α ranging from 60° to 210°) are considered here. The boundary conditions and fluid properties are similar to the above validation case in Section 3.1. The properties of the porous substrate are listed as follows, $k = 0.0039 l_L^2$, $\phi = 0.33$, and $t_{\text{Darcy}} = 68.16 t_L$, and the other material and model values are fixed here to highlight the influence of the tip geometry.

The time evolutions of liquid profiles of cases with different tip angle are given in Fig. 5. It is clearly seen that, for the cases with α of less than 180° (convex shape), the droplet can spread along the tip sides faster compared to that with a flat porous surface, and especially for the 60°, 75° and 90° cases, the droplet can be pierced by the tip. During its spreading process, the dry zones of the tip can be wetted immediately once the droplet touches due to the relatively high effective capillary suction which is a function of wetting-phase saturation. However, although the wetting-phase permeability increases since the pores are connected by wetting phase, effective capillary suction, as one of the driving factors for infiltration, goes down with the increment of saturation, and another driving factor is external pressure, which is positively related to the thickness of water film. Therefore, it is required to reduce the mobility of the droplet so that water can invade into the porous matrix more in terms of the penetration depth. To make such tendency clear, 90° cases with different bond number (Bo) are added as shown in Fig. 5(b). With the increment of Bo, the droplet mobility increases, i.e., the spreading length becomes longer; however, the infiltration depth decreases obviously at the same time.

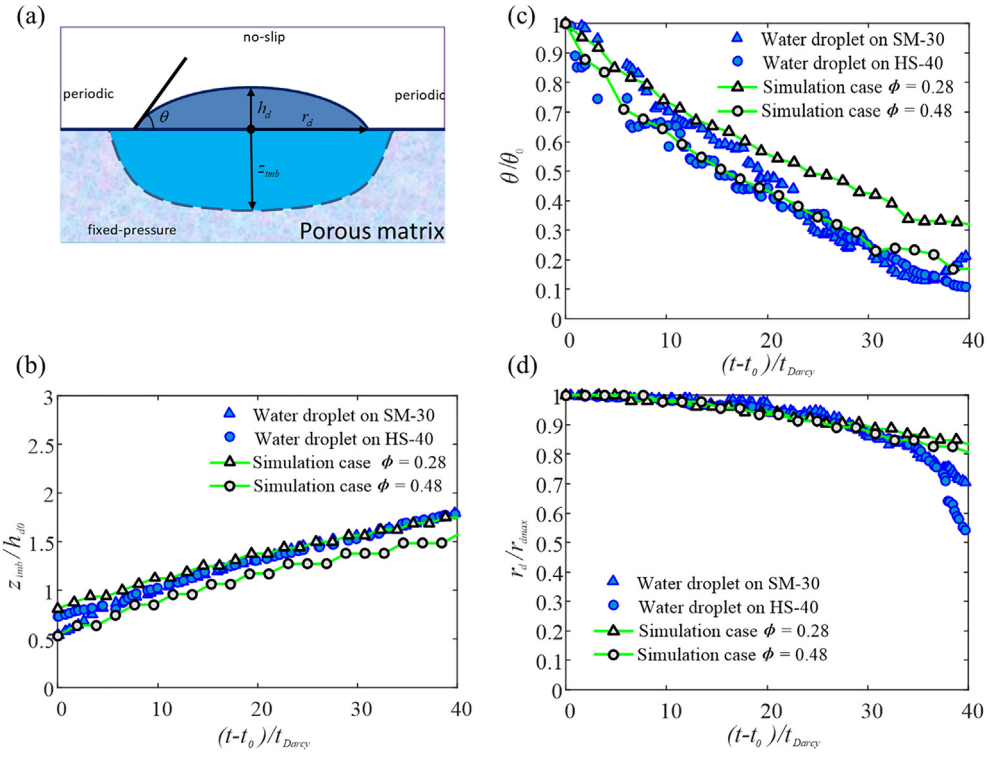

Fig. 3. (a) Schematic of a droplet on the porous matrix and the measured quantities including the apparent contact angle θ, droplet radius r_d, droplet height h_d, and vertical imbibition depth z_{imb}; (b-d) Dimensionless quantities, i.e., z_{imb}/h_{d0}, θ/θ_0 and $r_d/r_{d,\max}$, vs. scaled time $(t-t_0)/t_{\mathrm{Darcy}}$, respectively, where r_d reaches the maximum value $r_{d,\max}$ at time t_0.

Table 1
Parameters of two kinds uniform pore-throat networks.

	Permeability $k(l_L^2)$	Porosity ϕ (/)	Darcy's time t_{Darcy} (t_L)
Case 1 (SM-30 [13])	0.0079	0.28	154.67
Case 2 (HS-40 [13])	0.016	0.48	52.07

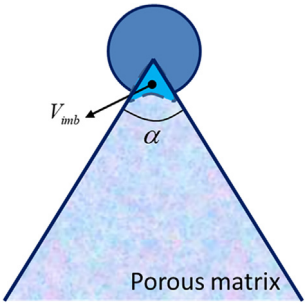

Fig. 4. The schematic of a droplet on a porous tip with inner angle of α, and V_{imb} indicates the infiltration volume.

To quantify the imbibition efficiency, two parameters, the *imbibition ratio* (the ratio of the infiltration volume and the initial droplet volume V_0) and the *relative spreading length* (the ratio of the spreading length and initial droplet diameter, as $d_0 = 2\sqrt{V_0/\pi}$ in 2D) are introduced here. The results are shown in Fig. 6(a) and (b), and overall these two quantities show similar tendencies over time and depend on the tip angle. However, the time evolutions do not show a monotonic response to the corresponding tip angle. Specifically, regarding both the time-varying imbibition efficiency and spreading length, the 75° case is better than 60° case, and 60° and 120° cases present the similar imbibition efficiency.

Fig. 7 shows the geometrical dependencies of the imbibition ratio and spreading length at the given time, $t/t_{\mathrm{Darcy}} = 100$. Obviously, sharper tip angle resulting in stronger downward sliding effect induced by the gravity, and such effect can promote the imbibition process when $\alpha \in (90^\circ, 210^\circ]$ since the droplet is driven to reach more dry surface areas; however, for a small enough tip angle $\alpha \in [60^\circ, 75^\circ)$, the deep penetration may impede the spreading process. The driving force for spreading depends on the gravity component, and thus we can expect different peak values for varying Bond number, which could be interesting for future work. As for the case with α larger than 180°, the droplet is trapped within a concave corner so that the spreading only depends on the surface hydrophilicity. Obviously, the increment of imbibition ratio resulted from spreading is more significant than that from pressure-driven suction because the pressure gradient decreases linearly with the liquid front moving further.

The above observations demonstrate a basic relationship between the inner tip angle and the droplet imbibition and spreading behaviour, and it may assist the optimised design of capillary-driven microfluidic devices, in which certain imbibition efficiency is required, such as medical chromatography (Sharma et al., 2018) and pharmaceutical tablet coating (Christodoulou et al., 2018).

This numerical framework is not only suitable for the issue regarding droplet on porous media but can also be further utilised in modelling more multiscale problems, such as multiphase flow in fractured rocks (Arshadi et al., 2018; Yinghao et al., 2018), where flow pathways of fractures and rock bodies have contrasting length

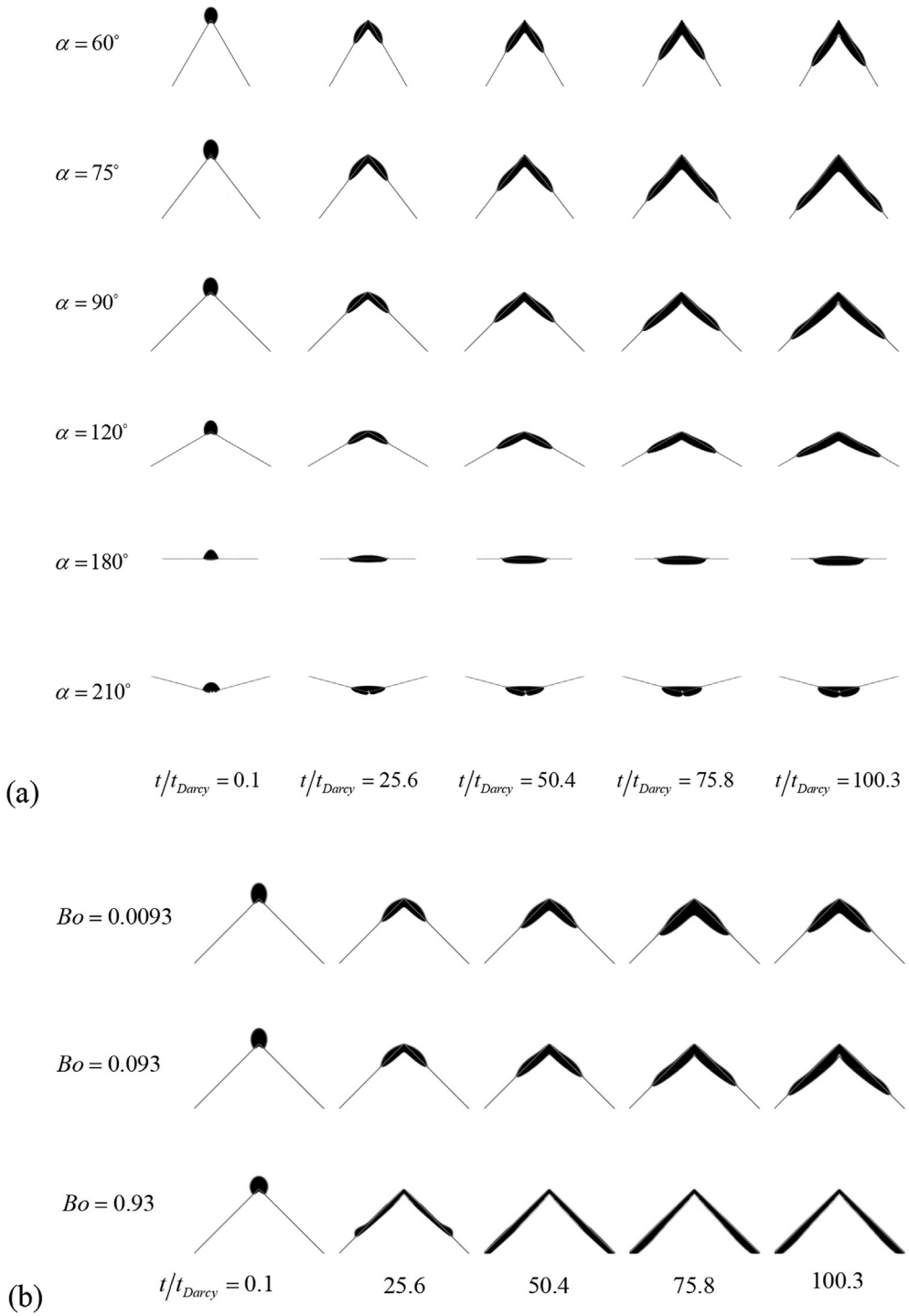

Fig. 5. Time evolution of liquid profiles, (a) cases with different tip angles α ranging from 60° to 210° at Bo = 0.093 (each column from top to bottom); (b) cases with different Bo ranging from 0.0093 to 0.93 at α = 90°.

scales. Another advantage of this numerical framework lies in that the wettability conditions of the porous surface and the inside of porous media can be considered separately. Therefore, the imbibition process in hydrophilic porous media with hydrophobic surfaces, such as braided fabrics (Espín and Kumar, 2015) and powders (Marston et al., 2010), can be described by this numerical method. Furthermore, it is relatively easy to extend the current 2D scheme to 3D due to the natural parallelisation of LBM and the topological simplicity of PNM.

4. Conclusions

For solving multiscale and multiphase flows, we developed a robust numerical framework concurrently coupling LBM and PNM and the novelty of this method is the interface treatment technique, i.e., two interacting flow domains with contrasting characteristic physical lengths are bridged, with the coarse-scale flows modelled by the PNM while fine-scale flows are modelled by the LBM. With this proposed numerical method, the droplet

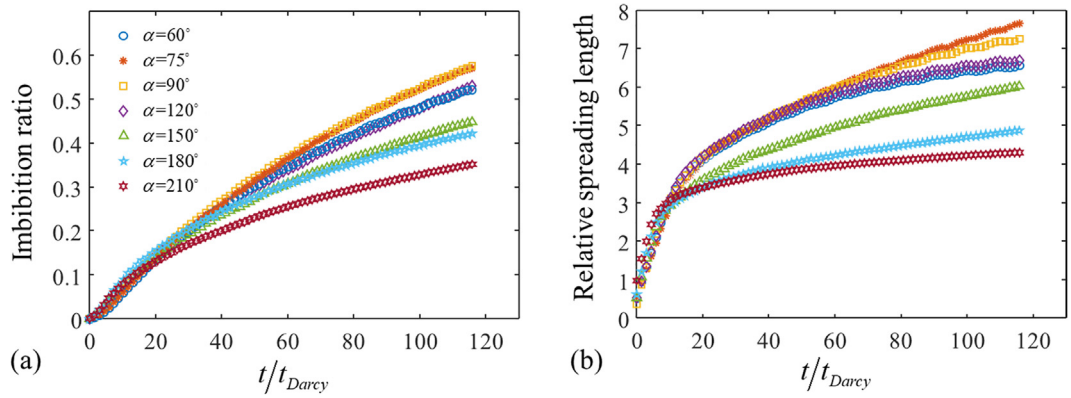

Fig. 6. (a) The ratio of the infiltration volume and the initial droplet volume, named imbibition ratio vs. scaled time t/t_{Darcy}; (b) the ratio of spreading length and initial droplet diameter, named relative spreading length vs. scaled time t/t_{Darcy}.

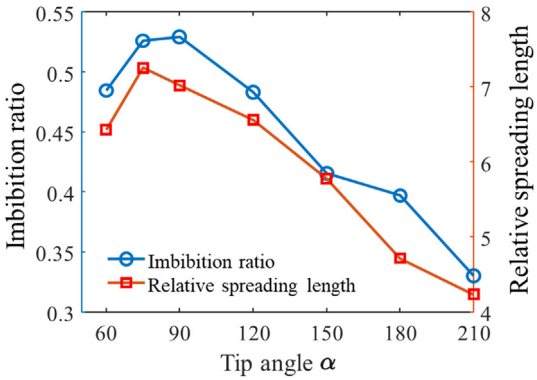

Fig. 7. Imbibition ratio and relative spreading length vs. tip angle at $t/t_{\text{Darcy}} = 100$.

spreading and imbibition on a flat porous surface are modelled and successfully validated against the available experimental observations. Moreover, by varying the geometry of non-flat interfaces, the competition between spreading over and imbibition into the porous medium is demonstrated. These results can assist the design of capillary-driven microfluidic devices, where the spreading behaviour on porous media may require quantitative controls. The proposed numerical framework provides a unique solution for multiphase flow in domains with two distinct length-scales and warrants further investigation on unravelling controlling mechanisms of the droplet dynamics on porous surfaces.

CRediT authorship contribution statement

Si Suo: Conceptualization, Methodology, Formal analysis, Visualization, Investigation, Writing - original draft. **Mingchao Liu:** Writing - review & editing. **Yixiang Gan:** Supervision, Conceptualization, Methodology, Writing - review & editing.

Declaration of Competing Interest

The authors declare that they have no known competing financial interests or personal relationships that could have appeared to influence the work reported in this paper.

Acknowledgements

This work was financially supported by Australian Research Council (Projects DP170102886) and The University of Sydney SOAR Fellowship. M.L. acknowledges the support from the Newton International Fellowship founded by the Royal Society. This research was undertaken with the assistance of resources and services from the HPC service at The University of Sydney. The authors would like to thank Professor Dominic Vella, from the Mathematical Institute at the University of Oxford, for his comments and feedbacks on this work.

Appendix. LBM-PNM coupling algorithm

The detailed algorithm of coupling technique can be referred in Table A1. For the function **LBM_collideAndStream**, streaming step as per Eq. (5), collision step as per Eqs. (7), (8), (16) and (17), and calculation of macro quantities as per Eqs. (10)–(12) are implemented. For the function **PNM_fixPressureAtInterface**, the Dirichlet boundary condition is applied at the interface for PNM domain, and only the wetting-phase pressure is passed from the LBM to PNM since single-pressure scheme is adopted in this study. Then, the pressure field is solved in the function **PNM_solve** as per Eq. (20), and the state of the pore-network is updated in **PNM_update** as per Eq. (21). Finally, the last component of a whole

Table A1
LBM-PNM coupling algorithm.

```
Algorithm: coupling LBM-PNM
//Initialize LBM domain and PNM domain;
  LBM_ini (); PNM_ini ();
  for t = 0:Δt:te //Δt is the step of LBM domain and te is the total simulation
  time length
    //Time step forward for LBM domain
    LBM_collideAndStream ();
    //Transfer the pressure to PNM domain at the interface
    PNM_fixPressureAtInterface (LBM_Pressure);
    t = 0 // time mark of PNM domain during Δt
    PNM_flowQuantityAtInterface = 0; //restore the flux values at the
  interface to zeros
    while t < Δt
      dt = Δt − t;
      // solve PNM domain and determine its time step dt
      dt_ = PNM_solve ();
      // update dt and t
      dt = min(dt_, dt); t += dt;
      // update the state of each pore and throat in PNM domain
      PNM_update (dt);
      // add the quantity flow at each interface node during dt
      PNM_flowQuantityAtInterface += dt·PNM_fluxAtInterface;
    end while
    PNM_ averageFluxAtInterface = PNM_ flowQuantityAtInterface / Δt;
    //Transfer the flux to LBM domain at the interface
    LBM_fixVelocityAtInterface (PNM_averageFluxAtInterface);
  end for
```

loop is the function **LBM_fixVelocityAtInterface**, where Eqs. (32) and (33) are implemented for the wetting phase. Notably, the bounce-back technique (Ladd and Verberg, 2001) is used here to apply interfacial velocity boundary in LBM since it is easy to treat the open boundaries not coinciding with the lattice directions.

References

Arshadi, M., Khishvand, M., Aghaei, A., Piri, M., Al-Muntasheri, G.A., 2018. Pore-scale experimental investigation of two-phase flow through fractured porous media.

Ba, Y., Liu, H., Li, Q., Kang, Q., Sun, J., 2016. Multiple-relaxation-time color-gradient lattice Boltzmann model for simulating two-phase flows with high density ratio. Phys. Rev. E 94. 023310.

Bakhta, Athmane, Leclaire, Sébastien, Vidal, David, Bertrand, François, Cheriet, Mohamed, 2019. Multiscale simulation of ink seepage into paper: A mesoscopic variational model. Comput. Phys. Commun. 239, 1–13. https://doi.org/10.1016/j.cpc.2019.02.001.

Bauer, D., Youssef, S., Fleury, M., Bekri, S., Rosenberg, E., Vizika, O., 2012. Improving the estimations of petrophysical transport behavior of carbonate rocks using a dual pore network approach combined with computed microtomography. Transp. Porous Media 94, 505–524.

Blunt, M.J., 2001. Flow in porous media — pore-network models and multiphase flow. Curr. Opin. Colloid Interface Sci. 6, 197–207.

Blunt, M.J., Bijeljic, B., Dong, H., Gharbi, O., Iglauer, S., Mostaghimi, P., Paluszny, A., Pentland, C., 2013. Pore-scale imaging and modelling. Adv. Water Resour. 51, 197–216.

Camuffo, D., 2013. Microclimate for Cultural Heritage: Conservation, Restoration, and Maintenance of Indoor and Outdoor Monuments. Elsevier.

Christodoulou, C., Sorensen, E., García-Muñoz, S., Mazzei, L., 2018. Mathematical modelling of water absorption and evaporation in a pharmaceutical tablet during film coating. Chem. Eng. Sci. 175, 40–55.

Clarke, A., Blake, T., Carruthers, K., Woodward, A., 2002. Spreading and imbibition of liquid droplets on porous surfaces. Langmuir 18, 2980–2984.

Daniel, R.C., Berg, J.C., 2006. Spreading on and penetration into thin, permeable print media: Application to ink-jet printing. Adv. Colloid Interface Sci. 123–126, 439–469.

Das, S., Patel, H., Milacic, E., Deen, N., Kuipers, J., 2018. Droplet spreading and capillary imbibition in a porous medium: A coupled IB-VOF method based numerical study. Phys. Fluids 30. 012112.

Denesuk, M., Zelinski, B.J.J., Kreidl, N.J., Uhlmann, D.R., 1994. Dynamics of incomplete wetting on porous materials. J. Colloid Interface Sci. 168, 142–151.

Espín, L., Kumar, S., 2015. Droplet spreading and absorption on rough, permeable substrates. J. Fluid Mech. 784, 465–486.

Frank, X., Perre, P., 2012. Droplet spreading on a porous surface: A lattice Boltzmann study. Phys. Fluids 24. 042101.

Fu, F., Li, P., Wang, K., Wu, R., 2019. Numerical simulation of sessile droplet spreading and penetration on porous substrates. Langmuir.

Ginzburg, I., Verhaeghe, F., d'Humieres, D., 2008a. Study of simple hydrodynamic solutions with the two-relaxation-times lattice Boltzmann scheme. Comm. Comput. Phys. 3, 519–581.

Ginzburg, I., Verhaeghe, F., d'Humieres, D., 2008b. Two-relaxation-time lattice Boltzmann scheme: About parametrization, velocity, pressure and mixed boundary conditions. Comm. Comput. Phys. 3, 427–478.

Gunstensen, A.K., Rothman, D.H., Zaleski, S., Zanetti, G., 1991. Lattice Boltzmann model of immiscible fluids. Phys. Rev. A 43, 4320.

Hsu, C.T., Cheng, P., 1990. Thermal dispersion in a porous medium. Int. J. Heat Mass Transf. 33, 1587–1597.

Huang, H., Huang, J.-J., Lu, X.-Y., 2014. Study of immiscible displacements in porous media using a color-gradient-based multiphase lattice Boltzmann method. Comput. Fluids 93, 164–172.

Huang, H., Wang, L., Lu, X.-Y., 2011. Evaluation of three lattice Boltzmann models for multiphase flows in porous media. Comput. Math. Appl. 61, 3606–3617.

Joekar-Niasar, V., Hassanizadeh, S.M., Dahle, H., 2010. Non-equilibrium effects in capillarity and interfacial area in two-phase flow: dynamic pore-network modelling. J. Fluid Mech. 655, 38–71.

Joekar-Niasar, V., Doster, F., Armstrong, R., Wildenschild, D., Celia, M., 2013. Trapping and hysteresis in two-phase flow in porous media: A pore-network study. Water Resour. Res. 49, 4244–4256.

Keiser, L., Keiser, A., L'Estimé, M., Bico, J., Reyssat, É., 2019. Motion of viscous droplets in rough confinement: paradoxical lubrication. Phys. Rev. Lett. 122. 074501.

Ladd, A.J.C., Verberg, R., 2001. Lattice-Boltzmann simulations of particle-fluid suspensions. J. Stat. Phys. 104, 1191–1251.

Latva-Kokko, M., Rothman, D.H., 2005. Static contact angle in lattice Boltzmann models of immiscible fluids. Phys. Rev. E 72. 046701.

Léang, M., Pauchard, L., Lee, L.-T., Giorgiutti-Dauphiné, F., 2019. Imbibition on a porous layer: dynamical and mechanical characterization. Soft Matter.

Leclaire, S., Reggio, M., Trépanier, J.-Y., 2013. Progress and investigation on lattice Boltzmann modeling of multiple immiscible fluids or components with variable density and viscosity ratios. J. Comput. Phys. 246, 318–342.

Levy, T., Sanchez-Palencia, E., 1975. On boundary conditions for fluid flow in porous media. Int. J. Eng. Sci. 13, 923–940.

Liu, H., Valocchi, A.J., Kang, Q., 2012. Three-dimensional lattice Boltzmann model for immiscible two-phase flow simulations. Phys. Rev. E 85. 046309.

Markicevic, B., Li, H., Sikorski, Y., Zand, A.R., Sanders, M., Navaz, H.K., 2009. Infiltration time and imprint shape of a sessile droplet imbibing porous medium. J. Colloid Interface Sci. 336, 698–706.

Markicevic, B., Navaz, H., 2010. Primary and secondary infiltration of wetting liquid sessile droplet into porous medium. Transp. Porous Media 85, 953–974.

Marston, J., Thoroddsen, S.T., Ng, W., Tan, R., 2010. Experimental study of liquid drop impact onto a powder surface. Powder Technol. 203, 223–236.

Meng, S., Yang, R., Wu, J.-S., Zhang, H., 2014. Simulation of droplet spreading on porous substrates using smoothed particle hydrodynamics. Int. J. Heat Mass Transf. 77, 828–833.

Neogi, P., Miller, C.A., 1983. Spreading kinetics of a drop on a rough solid surface. J. Colloid Interface Sci. 92, 338–349.

Oko, A., Martinez, D.M., Swerin, A., 2014. Infiltration and dimensional scaling of inkjet droplets on thick isotropic porous materials. Microfluid. Nanofluid. 17, 413–422.

Perazzo, A., Tomaiuolo, G., Preziosi, V., Guido, S., 2018. Emulsions in porous media: From single droplet behavior to applications for oil recovery. Adv. Colloid Interface Sci. 256, 305–325.

Pham, Q.N., Zhang, S., Montazeri, K., Won, Y., 2018. Droplets on slippery lubricant-infused porous surfaces: a macroscale to nanoscale perspective. Langmuir 34, 14439–14447.

Qin, C.-Z., Guo, B., Celia, M., Wu, R., 2019. Dynamic pore-network modeling of air-water flow through thin porous layers. Chem. Eng. Sci. 202, 194–207.

Reis, T., Phillips, T., 2007. Lattice Boltzmann model for simulating immiscible two-phase flows. J. Phys. A: Math. Theor. 40, 4033.

Rothman, D.H., Keller, J.M., 1988. Immiscible cellular-automaton fluids. J. Stat. Phys. 52, 1119–1127.

Shan, X., Chen, H., 1993. Lattice Boltzmann model for simulating flows with multiple phases and components. Phys. Rev. E 47, 1815–1819.

Sharma, N., Barstis, T., Giri, B., 2018. Advances in paper-analytical methods for pharmaceutical analysis. Eur. J. Pharm. Sci. 111, 46–56.

Starov, V.M., Zhdanov, S.A., Kosvintsev, S.R., Sobolev, V.D., Velarde, M.G., 2003. Spreading of liquid drops over porous substrates. Adv. Colloid Interface Sci. 104, 123–158.

Swift, M.R., Orlandini, E., Osborn, W., Yeomans, J., 1996. Lattice Boltzmann simulations of liquid-gas and binary fluid systems. Phys. Rev. E 54, 5041.

Tan, H., 2017. Absorption of picoliter droplets by thin porous substrates. AIChE J. 63, 1690–1703.

Thompson, K.E., 2002. Pore-scale modeling of fluid transport in disordered fibrous materials. AIChE J. 48, 1369–1389.

Valvatne, Per H., Blunt, Martin J., 2004. Predictive pore-scale modeling of two-phase flow in mixed wet media: PREDICTIVE PORE-SCALE MODELING. Water Resour. Res. 40 (7). https://doi.org/10.1029/2003WR002627.

Wang, M., Chen, Y.-F., Ma, G.-W., Zhou, J.-Q., Zhou, C.-B., 2016a. Influence of surface roughness on nonlinear flow behaviors in 3D self-affine rough fractures: Lattice Boltzmann simulations. Adv. Water Resour. 96, 373–388.

Wang, Z., Espín, L., Bates, F.S., Kumar, S., Macosko, C.W., 2016b. Water droplet spreading and imbibition on superhydrophilic poly(butylene terephthalate) melt-blown fiber mats. Chem. Eng. Sci. 146, 104–114.

Wijshoff, H., 2018. Drop dynamics in the inkjet printing process. Curr. Opin. Colloid Interface Sci. 36, 20–27.

Yin, X., Aslannejad, H., de Vries, E.T., Raoof, A., Hassanizadeh, S.M., 2018. Droplet imbibition into paper coating layer: pore-network modeling simulation. Transp. Porous Media 125, 239–258.

Yinghao, S., Ge, H., Zhang, X., Chang, L., Dunqing, L., Liu, J., 2018. Impact of fracturing liquid absorption on the production and water-block unlocking for shale gas reservoir.

Zhou, H., Chang, R., Reichmanis, E., Song, Y., 2017. Wetting of inkjet polymer droplets on porous alumina substrates. Langmuir 33, 130–137.